Global Monthly Ocean Dissolved Oxygen (1960 – 2023) Reconstructed to 5,902 m with BLENDR, a Bayesian-Optimized Ensemble Learning Framework

Mingyu Han[1], Xiaogang Xing[2], Yuntao Zhou[1]*

1. School of Oceanography, Shanghai Jiao Tong University, Shanghai, China

2. State Key Laboratory of Satellite Ocean Environment Dynamics (SOED), Second Institute of Oceanography, Ministry of Natural Resources, Hangzhou, China

Corresponding author

*Correspondence to: Yuntao Zhou, ytzhou@sjtu.edu.cn, ORCID: 0000-0001-9714-5385

Abstract

Oceanic oxygen levels, crucial for marine ecosystems and biogeochemical cycles, have declined significantly over the past few decades due to climate change, posing severe environmental risks. However, historical dissolved oxygen (DO) measurements, especially below 2,000 m, remain sparse, limiting comprehensive annual and seasonal analyses. Here, we introduce the BLENDR framework (Bayesian-optimized Learning and ENsemble modeling for Data Reconstruction), a Bayesian-optimized ensemble of six machine-learning models (Random Forest, XGBoost, LightGBM, CatBoost, Extremely Randomized Trees and Histogram-based Gradient Boosting) fused via dynamic weighting, to reconstruct global monthly DO distributions at a $1° \times 1°$ resolution from the surface to 5,902 m from 1960 to 2023. Validation against an independent dataset demonstrated that BLENDR achieves lower errors than any individual model. Our dataset captures depth-dependent deoxygenation, with the most pronounced decline occurring between 150 and 200 m, and reveals severely accelerated oxygen loss in the Arctic Ocean and North Atlantic over the past decade. This work provides the first long-term, global monthly DO product from the ocean surface to 5,902 m. The bathypelagic DO data provided in this work is a significant contribution to deep ocean oxygen dynamics and global biogeochemical cycles.

Keywords

dissolved oxygen, machine learning, ensemble learning, Bayesian optimization, data reconstruction

Earth System
Open Access Science
Data Discussions

1 Introduction

Over the past few decades, dissolved oxygen (DO) levels in open oceans have been rapidly decreasing (Breitburg et al., 2018; Keeling et al., 2010), primarily driven by climate change (Deutsch et al., 2011). This continuous decline has severely affected marine organisms and biogeochemical processes, disrupting marine productivity, biodiversity, and biogeochemical cycles (Gruber, 2011; Stramma et al., 2012). Climate models predict that global warming will further accelerate this deoxygenation (Oschlies et al., 2018), potentially adversely affecting aerobic marine organisms within this century (Sampaio et al., 2021) and altering biogeochemical cycles (Gruber, 2004; Berman-Frank et al., 2008). Therefore, it is important to develop a comprehensive, high-resolution reconstruction of ocean DO across both space and depth to accurately quantify historical deoxygenation trends, identify regional hotspots, and inform future ecosystem and climate projections.

Despite significant progress in oceanographic data collection, severe gaps in historical DO data persist, hindering comprehensive analysis. For instance, the World Ocean Database (WOD) (Mishonov et al., 2024) compiles DO profiles from research cruises and floats, yet most ocean regions still lack any observations. This sparse spatial coverage severely limits the use of data imputation methods to reconstruct four-dimensional DO fields. Furthermore, although many Earth System Models (ESMs) attempt to simulate global oceanic DO, these models lack adjustments based on DO observation data, leading to error propagation (Pathak et al., 2023). Thus, numerical models diverge significantly from *in situ* observations and consistently underestimate actual DO decline trends (Bopp et al., 2013; Cocco et al., 2013; Long et al., 2016; Kwiatkowski et al., 2020), which reduces confidence in model-based assessments of ocean deoxygenation, Oxygen Minimum Zones (OMZ), and biogeochemical cycles.

Classical interpolation methods have long been employed to map oceanic DO. Zhou et al. (2022) combined geostatistical regression with Monte Carlo methods to estimate changes in the area of OMZs globally and regionally from 1960 to 2019. Garcia et al. (2024) applied objective analysis in the World Ocean Atlas 2023 (WOA23) to produce internally consistent annual and monthly DO fields from 1965 to 2022. Gouretski et al. (2024) developed an automated quality control procedure to detect outliers and correct biases in ocean oxygen profiles, producing a consistent global dataset from 1920 to 2023. Roach and Bindoff (2023) used Data Interpolating Variational Analysis (DIVA) to generate a global high-resolution oxygen atlas from 1955 to 2018.

Recently, machine learning approaches have been increasingly adopted in Earth system science and oceanography because they can efficiently exploit large datasets and capture complex nonlinear relationships (Reichstein et al., 2019; Shen, 2018). Giglio et al. (2018) utilized a random forest regression model to estimate the oxygen concentration at 150 m in the Southern Ocean on the basis of Argo data from 2008 to 2012. Sharp et al. (2023) reconstructed a global DO dataset called GOBAI-O_2 using feedforward neural networks and random forest regression, spanning the years 2004–2022 with a monthly resolution and extending from the ocean surface to a depth of 2,000 m. Ito et al. (2024) developed a machine-learning ensemble of neural networks and random forests trained on historical shipboard and biogeochemical Argo DO profiles to generate

74 gridded monthly oxygen fields. Crucially, most existing machine-learning reconstructions are
75 limited to the upper 2,000 m of the water column, leaving the vast bathypelagic zone (below
76 2,000 m) poorly constrained, despite its importance for global carbon storage and long-term
77 oxygen budgets. While some of the DO data reconstruction studies focus on specific regions
78 (Giglio et al., 2018; Huang et al., 2023), some span longer time spans (Roach and Bindoff, 2023;
79 Ito et al., 2024), and some achieve higher temporal or spatial resolutions (Sharp et al., 2023; Shao
80 et al., 2023), it is challenging to simultaneously address all aspects.
81
82 Here, we introduce the BLENDR framework (Bayesian-optimized Learning and ENsemble
83 modeling for Data Reconstruction), which integrates six tree-based learners, Random Forest,
84 XGBoost, LightGBM, CatBoost, Extremely Randomized Trees and Histogram-based Gradient
85 Boosting, each tuned via Bayesian hyperparameter optimization. Model outputs are fused with
86 dynamic weights combining global cross-validation skill and local error performance. BLENDR
87 produces a global $1° \times 1°$ monthly DO dataset from 1960 to 2023 down to 5,902 m, filling
88 critical deep-ocean gaps. We evaluated the ensemble using 8-fold temporal cross-validation and
89 an independent subset of the Global Ocean Data Analysis Project v2.2023 (GLODAPv2) (Olsen et
90 al., 2016) after all the profiles that overlap with the WOD (CTD and OSD) collections were
91 removed to ensure independence. We also quantified the measurement, grid and algorithm
92 uncertainties. Using this product, we analyzed global, basin-scale and depth-resolved DO
93 distributions and long-term deoxygenation trends, including the vertical structure and
94 multi-basin evolution of OMZ extent, changes in basin-scale oxygen content and their recent
95 acceleration, and hemispheric differences in DO seasonality. In addition, we quantified the
96 influence of a recently documented systematic bias in delayed-mode Argo DO by comparing
97 reconstructions with and without a system correction applied to Argo profiles. To capture
98 regional differences in oxygen storage and trends, we divided the global ocean into ten basins:
99 the North Pacific (NP), Equatorial Pacific (EP), South Pacific (SP), North Atlantic (NA), Equatorial
100 Atlantic (EA), South Atlantic (SA), North Indian (NI), South Indian (SI), Southern Ocean (SO) and
101 Arctic Ocean (AO). The basin boundaries (Figure 1) follow Schmidtko et al. (2017).
102

103 ## 2 Data and methods

104 ### 2.1 Data
105 ### 2.1.1 Observational data of dissolved oxygen

106 We assembled our observational DO database by merging quality-controlled profiles from the
107 Array for Real-Time Geostrophic Oceanography dataset (Argo, https://argo.ucsd.edu) (Wong et al.,
108 2020) with Conductivity-Temperature-Depth (CTD) and Ocean Station Data (OSD) measurements
109 archived in the World Ocean Database 2023 (WOD,
110 https://www.ncei.noaa.gov/products/world-ocean-database) (Mishonov et al., 2024). Each
111 profile consists of oxygen concentrations sampled at multiple depths at a given date and location.
112 For Argo, we restricted the data to post-processed delayed-mode profiles and retained only
113 records flagged as good. Overlapping profiles were deduplicated by keeping the version with
114 finer vertical sampling. Although we initially followed Schmidtko et al. (2017) in treating the
115 combined dataset as free of systematic errors, recent evidence indicates a systematic offset

116 between Argo and CTD/OSD. Accordingly, following Wang et al. (2025), we applied a uniform
117 +1.69 µmol kg^{-1} bias correction to all delayed-mode Argo DO profiles.

118 To obtain an independent evaluation set, we constructed a validation subset from GLODAPv2
119 (Olsen et al., 2016) after removing any profiles that overlap with our training pool from CTD and
120 OSD. We compared the two collections profile by profile and applied a conservative space and
121 time filter: for each oxygen profile in GLODAPv2, we searched the CTD and OSD records for
122 profiles within $\pm 1°$ in longitude, $\pm 1°$ in latitude, and the same calendar month. When
123 such a match existed, we treated the pair as duplicates and excluded the GLODAPv2 profile from
124 validation. This reduced the original 56,480 GLODAPv2 profiles to 8,020. A manual spot check
125 confirmed that no additional space-time matches remained. We therefore use this filtered
126 GLODA v2 set as a robust and independent benchmark for assessing our reconstruction.

127 **2.1.2 Reanalysis data of environmental factors**
128 We obtained monthly ocean temperature (T, °C), salinity (S, PSU), meridional velocity and zonal
129 velocity (MV and ZV, m s^{-1}) from the Ocean Reanalysis System 5 (ORAS5) gridded ocean dataset
130 with a spatial resolution of 0.25$°$ $\times$ 0.25$°$ and 75 vertical levels (Table S1), ranging from the
131 ocean surface to 5902 m in depth (https://cds.climate.copernicus.eu/datasets/reanalysis-oras5).
132
133 **2.2 BLENDR framework**
134 We developed the BLENDR framework to reconstruct a global, monthly DO product from 1960
135 through 2023. The process began by assembling and preprocessing all available *in situ* DO profiles
136 alongside key environmental factors (T, S, and currents) onto a monthly grid featuring a 1$°$ $\times$ 1$°$
137 horizontal resolution and 75 vertical levels. Next, each of the six tree-based learners (Random
138 Forest, XGBoost, LightGBM, CatBoost, Extremely Randomized Trees and Histogram-based
139 Gradient Boosting) underwent Bayesian hyperparameter tuning via Optuna's TPE sampler,
140 ensuring that each model minimized the cross-validation RMSE (Akiba et al., 2019). Once
141 optimized, the models were trained on the full gridded dataset and predicted the DO
142 concentration at every valid grid cell, producing six complete four-dimensional DO fields. These
143 outputs were then merged through a dynamic weighting scheme (Dietterich, 2000). This
144 approach uses prior weights based on each model's time-cross-validation skill and adjusts them
145 locally with "dynamic" weights that reflect agreement with nearby observations, yielding an
146 ensemble that adapts in space and time. Finally, we validated and quantified the performance by
147 conducting 8-fold temporal cross-validation, an independent evaluation against GLODAPv2 (Olsen
148 et al., 2016).
149 **2.2.1 Data processing**
150 In this study, all ocean DO observation data included temporal and spatial information, such as
151 the year, month, day, longitude, latitude, and measurement depth. The longitude and month are
152 both periodic features. For instance, longitude ranges from 0$°$ to 360$°$, with 360$°$
153 overlapping with 0$°$, and month indexes an annual cycle that repeats every 12 months. To
154 address this issue, we followed the approach of Gade (2010) and Tang et al. (2019) by converting
155 the longitude and month attributes to polar coordinate systems using sine and cosine functions.
156 Although ORAS5 is provided on a 0.25$°$ $\times$ 0.25$°$ grid, we upscaled it by simple averaging to a
157 common 1$°$ $\times$ 1$°$ grid with 75 depth levels. For each 1$°$ cell, we took the mean of the 16
158 underlying 0.25$°$ cells. DO observations are binned to each grid cell by averaging all points that

159 fall within the cell at the same month and depth level. To address potential multicollinearity,
160 which can lead to instability in subsequent modeling and increase the risk of overfitting, we
161 analyzed correlations between the 11 factors. No correlation coefficient exceeded 0.5, so variable
162 selection was not necessary in this case (Figure S2). A complete list of predictors, with
163 abbreviations and data sources, is shown in Table 1.

164 **Table 1. Predictors, abbreviations and products/references of the 11 environmental factors.**

Predictor	Abbreviation	Product/Reference
$\sin(\text{latitude}\cdot\pi/180)$	coord_1	WOD (CTD+OSD) & Argo
$\sin(\text{longitude}\cdot\pi/180)\cdot\cos(\text{latitude}\cdot\pi/180)$	coord_2	
$-\cos(\text{longitude}\cdot\pi/180)\cdot\cos(\text{latitude}\cdot\pi/180)$	coord_3	
Year	Year	
$\cos(\text{month}\cdot2\pi/12)$	time_cos	
$\sin(\text{month}\cdot2\pi/12)$	time_sin	
Depth	Depth	
Temperature	T	ORAS5
Salinity	S	
Zonal Velocity	ZV	
Meridional Velocity	MV	

165 Note: The observational data were from WOD and Argo. The data from ORAS5 were 0.25° ×
166 0.25° monthly mean profile data.

167

168 **2.2.2 Machine learning models**

169 We used six tree- based algorithms to reconstruct dissolved oxygen. Each model offers a different
170 balance of bias, variance, and speed. We chose them because of their robust performance in
171 regression tasks and their ability to handle nonlinear relationships. We used six models because
172 they span the main tree learning paradigms, namely, bagging and boosting; thus, their strengths
173 are complementary, and their residual errors are only weakly correlated. We kept the ensemble
174 within the tree family because dissolved oxygen depends on nonlinear interactions among
175 multiple drivers, and the data contain missing values, which are conditions in which decision
176 trees perform well without elaborate feature engineering. In preliminary trials with neural
177 networks, we did not observe a consistent increase in skill, whereas interpretability and tuning
178 became more difficult; thus, the tree ensemble offered the best balance for this application. All
179 the models were trained on the same input features and tuned via Bayesian optimization
180 (Sect. 2.2.3). Below, we describe each model.

181 Random Forest (RF) builds many decision trees on bootstrap samples and averages their outputs
182 (Breiman, 2001). It selects a random subset of features at each split. This randomness reduces
183 overfitting. RF handles large datasets well and is robust to outliers. RF represents classical
184 bagging, and Extremely Randomized Trees (ERTs) push this idea toward stronger randomness
185 (Geurts et al., 2006). It selects split thresholds at random rather than searching for the best cut. It
186 uses the full dataset rather than bootstrapping. This strong randomization further lowers
187 variance at modest cost in terms of bias. CatBoost is a gradient-boosting library designed for
188 categorical features (Prokhorenkova et al., 2018). It uses ordered target statistics to avoid target

189 leakage. It grows symmetric trees and performs efficient leaf pruning. CatBoost often converges
190 faster and requires less tuning of the learning rate. XGBoost implements gradient boosting with
191 second-order optimization (Chen & Guestrin, 2016). It adds regularization to control the
192 complexity of the tree. It uses approximate split finding to speed up training on large data.
193 XGBoost balances accuracy and runtime efficiency. LightGBM uses histogram-based binning and
194 leaf-wise tree growth (Ke et al., 2017). It buckets continuous features into bins, reducing the
195 amount of memory. Trees grow by selecting splits that yield the greatest loss reduction.
196 LightGBM is highly efficient for large feature sets and large datasets. Histogram-based Gradient
197 Boosting (Hist_GBT) follows Friedman's original gradient boosting framework (Guryanov, 2019;
198 Friedman, 2001). It fits a sequence of weak learners to the negative gradient of the loss. It also
199 uses histogram binning for faster split evaluation. Hist_GBT offers good accuracy in
200 high-dimensional settings. XGBoost, LightGBM and Hist_GBT are gradient boosting methods but
201 differ in terms of split criteria and optimization details.

202 **2.2.3 Bayesian parameter optimization**

203 To optimize hyperparameters across different machine learning models in a systematic and
204 efficient manner, we employed Bayesian optimization using the Optuna framework (Akiba et al.,
205 2019). Unlike grid or random search, this approach builds a statistical model of how settings
206 affect error and then tests promising regions more often, finding good configurations with fewer
207 trials and providing a fair, comparable procedure across models. Specifically, at each trial, a
208 candidate set of hyperparameters is sampled, the model is trained, and its validation error is
209 recorded. Optuna then uses all the previously tested hyperparameter–error pairs to update the
210 surrogate model and proposes the next set of hyperparameters where the error is expected to
211 decrease.

212 Bayesian optimization was used to construct a probabilistic surrogate model of the objective
213 function f(x), where x is a vector of hyperparameters. The optimization seeks to identify the
214 optimal x* that minimizes f:

215 $$\mathbf{x}^* = \arg\min_{x \in \chi} f(x) \tag{1}$$

216 Here, χ denotes the hyperparameter space. In practice, we used the Tree-structured Parzen
217 Estimator (TPE) sampler in Optuna to approximate the objective function. After each trial, the
218 observed pairs (x, f(x)) are divided into a "good" set with low objective values and a "bad" set
219 with high values, using a quantile threshold. The TPE then fits two probability density functions
220 over the hyperparameters, one for the good set and one for the bad set, and proposes new
221 candidates in regions where the ratio of these densities is large. This strategy is equivalent to
222 selecting the next sampling point to maximize the Expected Improvement (EI):

223 $$EI(X) = \int_{-\infty}^{y*} (y* - y) \cdot p(y \mid x) dy \tag{2}$$

224   where y* is the current best objective value. The sampling focuses on regions with high EI. In

225   plain terms, the EI favors trials that are expected to reduce the error relative to the current best,

226   so the search is concentrated on the most promising parts of the space.

227   To reduce temporal overfitting and preserve model generalizability across decades,

228   hyperparameter optimization was conducted using a subset of data from eight years (1960, 1968,

229   1976, 1984, 1992, 2000, 2008, 2016). These years were chosen to sample different climate and

230   sampling regimes across the six-decade period, ensuring that the optimized models are robust to

231   temporal shifts in data availability and underlying oceanic conditions. The objective function

232   minimized the Mean Squared Error (MSE) on an independent validation set derived from eight

233   other test years (1967, 1975, 1983, 1991, 1999, 2007, 2015, and 2023). We chose the MSE

234   because it penalizes large errors more heavily, which is desirable when evaluating gridded oxygen

235   where occasional large deviations can dominate downstream diagnostics. The objective function

236   was defined as follows:

237
$$MSE = \frac{1}{n}\sum_{i=1}^{n}(\hat{y}_i - y_i)^2 \tag{3}$$

238   Each model was optimized over its own hyperparameter space, with the best-performing

239   configuration recorded for final training and subsequent prediction on independent test data.

240   This consistent, data-driven approach ensured fair comparability across all six learners and

241   minimized bias from manual tuning. Below, we summarize the search space and optimal

242   parameters in Table 2.

243   **Table 2. Hyperparameter search spaces and optimal values**

Model	Hyperparameter	Search Range	Best Value
ERT	n_estimators	50 – 500	452
	max_depth	3 – 20	20
	min_samples_split	2 – 20	15
	min_samples_leaf	1 – 10	2
	max_features	0.1 – 1.0	0.577
	bootstrap	{True, False}	False
CatBoost	iterations	50 – 1000	950
	depth	3 – 12	12
	learning_rate	0.005 – 0.3	0.077
	l2_leaf_reg	10^{-5} – 10	0.009
	random_strength	10^{-5} – 10	7.053×10^{-5}
	bagging_temperature	0 – 1	0.122
	border_count	32 – 255	120
Hist_GBT	learning_rate	0.005 – 0.3	0.177
	max_iter	50 – 1000	928
	max_depth	3 – 12	8
	min_samples_leaf	5 – 50	41
	l2_regularization	10^{-5} – 10	0.932

Earth System
Science
Data

Open Access   Discussions

	max_bins	32 – 255	251
LightGBM	n_estimators	50 – 1000	954
	max_depth	3 – 12	12
	learning_rate	0.005 – 0.3	0.264
	num_leaves	10 – 300	145
	min_child_samples	5 – 50	18
	subsample	0.5 – 1.0	0.683
	colsample_bytree	0.5 – 1.0	0.828
	reg_alpha	10^{-8} – 10	6.15×10^{-7}
	reg_lambda	10^{-8} – 10	4.708
RF	num_trees	10 – 200	87
	min_leaf_size	10 – 100	10
XGBoost	n_estimators	50 – 1000	138
	max_depth	3 – 12	12
	learning_rate	0.005 – 0.3	0.256
	min_child_weight	1 – 10	5
	subsample	0.5 – 1.0	0.922
	colsample_bytree	0.5 – 1.0	0.599

244

245 **2.2.4 Multi-model fusion and dynamic weighting strategy**

246 We fused the six model predictions into one field. Our goal was to combine global model skill

247 with local fit to observations. We assigned each model a static "prior" weight. The prior serves as

248 a baseline that reflects each model's average skill over time and space and provides a stable

249 fallback where observations are sparse or absent; thus, the fusion does not chase noise in poorly

250 sampled regions. We then adjusted those weights at each grid cell using the local agreement

251 between the prediction and observation. This second step allows for nearby observations to steer

252 the fusion so that, where data exist, models that match them contribute more.

253 We derive a prior weight ω_i for Model i from its time-cross-validation (Sect. 3.1) RMSE ε_i. We set

254 a decay parameter β. Then,

255
$$\omega_i = \frac{\exp(-\beta \varepsilon_i)}{\sum_{j=1}^{6} \exp(-\beta \varepsilon_j)}, \sum_{i=1}^{6} \omega_i = 1 \qquad (4)$$

256 A smaller ε_i yields a larger ω_i. We chose β=1 to balance the influence among the models. β

257 controls how quickly low-error models dominate, and β=1 rewards better performers without

258 collapsing diversity.

259 At each grid cell x, we compute a dynamic weight $v_i(x)$. We use a tuning parameter α. For cells

260 where an observation O(x) exists, we set the following equation:

261
$$v_i(x) = \exp(-\alpha \, | \, p_i(x) - O(x) \, |) \qquad (5)$$

262 Here, $p_i(x)$ is model i's prediction. A smaller local error makes $v_i(x)$ larger. We used α=1. The

263 parameter α indicates how strongly local mismatch reshapes the weights, and $\alpha=1$ provided

264 the best trade-off between responsiveness to local observations and stability in cross-validation

265 tests. For cells with no observation, we used the static weight as follows:

266 $$v_i(x) = \omega_i \tag{6}$$

267 We computed the ensemble prediction E(x) by normalizing the dynamic weights:

268 $$E(x) = \frac{\sum_{i=1}^{6} v_i(x) p_i(x)}{\sum_{i=1}^{6} v_i(x)}, if \sum_i v_i(x) > 0 \tag{7}$$

269 and E(x)=NaN if all $p_i(x)$ are missing. This formula guarantees that models aligning well with local

270 observations gain more influence, while the static weights keep poorly observed regions stable.

271 **2.2.5 Data reconstruction**

272 We produced a global, monthly DO dataset on a regular $1° \times 1°$ grid and 75 depth levels

273 (0–5902 m) spanning from 1960 to 2023. First, we gathered all the predictor fields described in

274 Table 1. Each field was remapped to the target grid and monthly time step following ORAS5. Next,

275 we applied the six optimized machine-learning models (Sect. 2.2.2) at every valid grid cell and

276 time. Each model ingested the full vector of predictors and returned a DO estimate only where all

277 the predictors were present. This yielded six parallel prediction arrays with dimensions 360

278 (longitude) $\times$ 180 (latitude) $\times$ 75 (depth levels) $\times$ 12 (months) $\times$ 64 (years from 1960 to

279 2023). We then merged these arrays using our dynamic weighting scheme (Sect. 2.2.4). Static

280 "prior" weights reflect each model's cross-validation skill. Local weights adapt to agree with any

281 overlapping *in situ* observations. The weighted combination produces a single ensemble DO field

282 at each grid cell and month. We packaged the ensemble field into a NetCDF file with coordinate

283 variables, depth layers, time axes, and global attributes documenting the data and methods.

284 **2.2.6 Argo oxygen data bias correction**

285 Even after delayed-mode processing and standard quality control, Argo DO profiles are known to

286 be systematically low relative to high-quality ship-based observations. To quantify the influence

287 of a systematic offset in delayed-mode Argo, we produced two global reconstructions using the

288 same machine-learning framework and predictors. The first was a standard reconstruction using

289 CTD, OSD, and delayed-mode Argo profiles. The second was the bias-corrected reconstruction,

290 which was otherwise identical but utilized the CTD, OSD, and delayed-mode Argo values adjusted

291 by adding 1.69 µmol kg^{-1} to every delayed-mode Argo measurement, following Wang et al. (2025).

292 A comparison of the two reconstructions is shown in Section 4.4. All the other main results of the

293 paper are based on the bias-corrected reconstruction.

294 # 3 Model performance

295 **3.1 Model temporal cross- validation**

296 We conducted 8-fold temporal cross-validation on each of the six models. In each fold f, data

297 from eight test years $\{1960 + f + 8k\}_{k=0}^{7}$ formed the test set, with the remaining years for

298 training. We trained each model using its optimized hyperparameters (Sect. 2.2.3) on the training

299 set, predicted the DO values for the test years, and computed the mean bias (ΔDO), mean

300 absolute error (MAE), root-mean-square error (RMSE), and coefficient of determination (R^2) on
301 the held-out data. These metrics collectively provide a comprehensive understanding of the
302 model's predictive accuracy and bias. The results are presented in Tables S2–5.

303
$$RMSE = \sqrt{\frac{1}{n}\sum_{i=1}^{n}(y_i - \hat{y}_i)^2}$$
(8)

304
$$MAE = \frac{1}{n}\sum_{i=1}^{n}|y_i - \hat{y}_i|$$
(9)

305
$$R^2 = 1 - \frac{\sum_{i=1}^{n}(y_i - \hat{y}_i)^2}{\sum_{i=1}^{n}(y_i - \overline{y})^2}$$
(10)

306
$$\Delta DO = \frac{1}{n}\sum_{i=1}^{n} y_i - \hat{y}_i$$
(11)

307 All six learners exhibited consistent skill across the eight temporal folds, with only minor spread
308 in error metrics (Table S3-6). LightGBM displayed high stability, with MAEs varying by less than 1
309 µmol kg⁻¹ (10.11–11.04) and RMSEs under 1.3 µmol kg⁻¹ (16.38–17.59), yielding an R² range of
310 0.957–0.961. RF delivered the lowest RMSE (15.97–17.27) and highest R² (0.958–0.963). In
311 contrast, CatBoost and Hist_GBT had slightly higher mean errors (MAEs of up to 11.04 and 11.42
312 and RMSEs of up to 17.57 and 17.99, respectively) and slightly greater inter-fold variability,
313 indicating higher sensitivity to the specific training/test split (Table S2-5). Crucially, no model
314 exhibited outlier folds with degraded performance, as all the models maintained MAEs < 12 µmol
315 kg⁻¹ and R² > 0.95. This uniformity across folds confirms strong temporal generalization and
316 validates our choice of an ensemble approach (Bergmeir & Benítez, 2012; Roberts et al., 2017).

317 **3.2 Evaluation against independent observations**
318 We evaluated both the ensemble and each single model against an independent filtered
319 GLODAPv2 dissolved oxygen dataset, treated here as ground truth. Filtered GLODAPv2 profiles
320 were averaged into the same 1° × 1° grid and monthly time step as the reconstructions.

321 **Table 3. Comparison of ensemble and single models on the filtered GLODAPv2 dataset**

Model	MAE (µmol kg⁻¹)	RMSE (µmol kg⁻¹)	R²	Δ DO (µmol kg⁻¹)
Ensemble	**10.238**	**18.170**	**0.967**	-0.296
Ensemble(static weight=1)	10.434	18.302	0.967	-0.214
RF	10.266	18.394	0.966	-0.531
XGBoost	12.136	19.502	0.962	0.270
ERT	11.402	19.620	0.962	-1.167
LightGBM	11.314	18.968	0.964	0.167
Hist_GBT	11.942	19.739	0.962	**-0.099**
CatBoost	11.549	19.275	0.963	0.431

322 Table 3 demonstrates the clear advantage of the BLENDR framework. While an equal-weight
323 ensemble (static weight = 1) outperformed most single models, our RMSE-based dynamic weight
324 further improved accuracy, achieving the lowest overall errors. This demonstrates that leveraging
325 each learner's cross-validation skill yields a measurably better ensemble than equal weighting
326 does. Among the individual algorithms, the RF and LightGBM performed best, whereas XGBoost
327 and Hist_GBT performed at the lower end. All the models maintained the bias under 0.6 µmol
328 kg⁻¹. No single method showed unstable or extremely poor performance in this evaluation,
329 underscoring the robustness of our dynamic weighting in combining complementary strengths
330 and minimizing weaknesses.

331

332 **3.3 Uncertainty estimations**
333 We quantified three distinct contributors to uncertainty in the reconstructed DO field, namely,
334 measurement, grid, and algorithm uncertainty. These components were estimated separately
335 and then combined to provide a first-order global uncertainty estimate.

336

337 The measurement uncertainty ($\triangle O_{meas}$) represents the random errors of the *in situ* dissolved
338 oxygen observations. We adjusted the delayed-mode Argo DO values by adding a constant +1.69
339 µmol kg⁻¹ (Sect. 2.1.1), following the global bias assessment of Wang et al. (2025). After this bias
340 correction, we treated Argo and CTD/OSD as unbiased on average, and $\triangle O_{meas}$ represents only
341 the residual random measurement error. We assumed constant uncertainties of 1 µmol kg⁻¹ for
342 OSD and CTD and 3 µmol kg⁻¹ for Argo, following Ito et al. (2024). We then summarized a
343 representative value across all observations using the root-mean-square of these assigned
344 uncertainties.

345

346 The grid uncertainty ($\triangle O_{grid}$) quantifies the error associated with assigning a single value to a
347 1°×1° grid cell. We estimated $\triangle O_{grid}$ from the dispersion of collocated observations within each
348 grid cell. For each grid cell with at least 10 collocated observations, we computed the within-cell
349 standard deviation as follows:

350
$$\Delta O_{\text{grid}} = \sigma = \sqrt{\frac{1}{n-1}\sum_{i=1}^{n}(O_i - \overline{O})^2} \tag{12}$$

351 where O_i is the i-th observation in the cell and $\overline{O}$ is the mean value of the observations. We
352 then averaged σ over all qualifying cells to obtain a single global estimate of $\triangle O_{grid}$.

353

354 The algorithm uncertainty ($\triangle O_{alg}$) reflects the error introduced by the machine learning
355 reconstruction process. We trained six models (RF, XGBoost, LightGBM, CatBoost, ERT, and
356 Hist_GBT) using DO observations and environmental factors. Each model was optimized via
357 Bayesian hyperparameter tuning and validated using an 8-fold cross-validation procedure,
358 yielding an MAE for each model, denoted by error₁ through error₆. We then computed the prior
359 weight for the i-th model using an exponential decay function:

360
$$\omega_{\text{i}} = \frac{\exp(-error_i)}{\sum_{j=1}^{6}\exp(-error_j)}. \tag{13}$$

361 and estimated the algorithm uncertainty as the weighted average of the MAE:

362
$$\Delta O_{alg} = \sum_{i=1}^{6} \omega_i error_i .$$
(14)

363 Finally, the total uncertainty (ΔO_{total}) in the reconstructed dissolved oxygen field is expressed as
364 follows:

365
$$\Delta O_{total} = \sqrt{\Delta O_{meas}^2 + \Delta O_{grid}^2 + \Delta_{alg}^2}$$
(15)

366

367 Using this framework, the estimated global component uncertainties were Δ
368 O_{meas} = 1.60 µmol kg^{-1}, ΔO_{grid} = 4.56 µmol kg^{-1}, and ΔO_{alg} = 10.29 µmol kg^{-1}, resulting in a
369 combined global uncertainty of ΔO_{total} = 11.37 µmol kg^{-1}.

370

371 4 Global ocean DO distribution and trends

372 4.1 Spatial distributions along the vertical direction
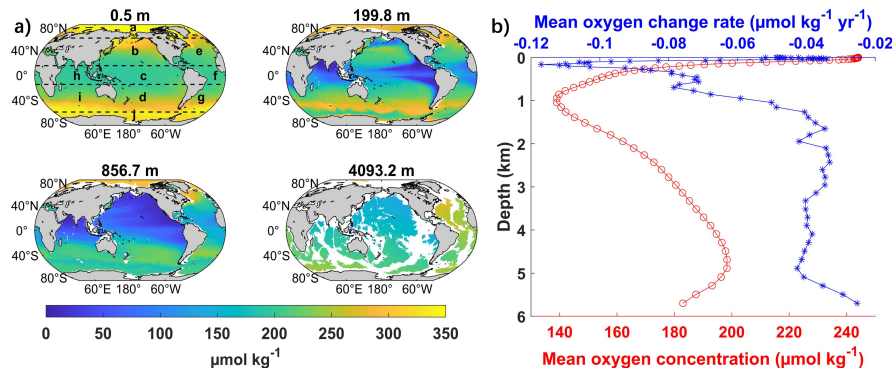
374 **Figure 1. Global distribution and vertical structure of dissolved oxygen.** (a) Climatological mean dissolved oxygen
375 concentration at four representative depths (0.5 m, 199.8 m, 856.7 m, and 4,093.2 m) from the reconstructed
376 global product. Letters indicate the ten regions: a) Arctic Ocean (AO), b) North Pacific (NP), c) Equatorial Pacific
377 (EP), d) South Pacific (SP), e) North Atlantic (NA), f) Equatorial Atlantic (EA), g) South Atlantic (SA), h) Equatorial
378 Indian (EI), i) South Indian (SI), and j) Southern Ocean (SO). This regionalization scheme is adopted from
379 Schmidtko et al. (2017). (b) Global mean vertical profiles of the dissolved oxygen concentration (red; µmol kg^{-1})
380 and its long-term linear change rate (blue; µmol kg^{-1} yr^{-1}).

381

382 Our reconstruction shows the full vertical extent of historical deoxygenation from the surface
383 ocean to the abyss, providing continuous monthly fields down to 5,902 m (Figure 1a). The surface
384 layer (0.5 m) is generally characterized by high DO concentrations, reflecting air–sea exchange
385 and photosynthetic production (Ryther, 1956; Kolber et al., 2000). The especially high values at
386 high latitudes (> 300 µmol kg^{-1}) are consistent with enhanced oxygen solubility in colder waters.
387 At approximately 200 m, strong horizontal contrasts emerge, with broad low-oxygen regions in
388 the eastern tropical Pacific and northern Indian Ocean (< 160 µmol kg^{-1}), while relatively
389 oxygenated in subpolar zones (> 200 µmol kg^{-1}). This rapid decrease reflects diminished gas

Earth System
Science
Data
Open Access
Discussions

390 exchange and ongoing microbial respiration (Keeling et al., 2010; Schmidtko et al., 2017). At
391 approximately 850 m, the lowest DO concentrations are most evident, with the concentrations in
392 the eastern Pacific and northern Indian Ocean decreasing below 150 µmol kg^{-1}, whereas the
393 North Atlantic (NA) mid-depth ocean maintains higher concentrations (180–200 µmol kg^{-1}). In the
394 bathypelagic zone (~4,000 m), DO becomes spatially uniform (180–200 µmol kg^{-1}) across basins,
395 which is consistent with the large-scale deep-water mass structure (Talley, 2013). Overall, along
396 the water column, the DO concentration peaks at the surface and reaches a local minimum of
397 approximately 139 µmol kg^{-1} near the classical OMZ at approximately 1,000 m but then slowly
398 increases toward 200 µmol kg^{-1} at approximately 4,500 m (Figure 1b).
399

400 The global mean DO trend from 1960 to 2023 was negative at nearly all depths, with the
401 strongest deoxygenation in the subsurface ocean and weaker trends in the surface and deep
402 ocean (Figure 1b). While the deoxygenation rate was low (-0.04 µmol kg^{-1} yr^{-1}) at the surface, the
403 decline accelerated greatly below 60 m, reaching its most negative values between 150 and 200
404 m (-0.12 µmol kg^{-1} yr^{-1}). This pattern reflects an amplification of shallow subsurface oxygen loss,
405 most likely driven by stronger stratification that inhibits ventilation exchange and by increased
406 microbial respiration (Keeling et al., 2010; Schmidtko et al., 2017).
407

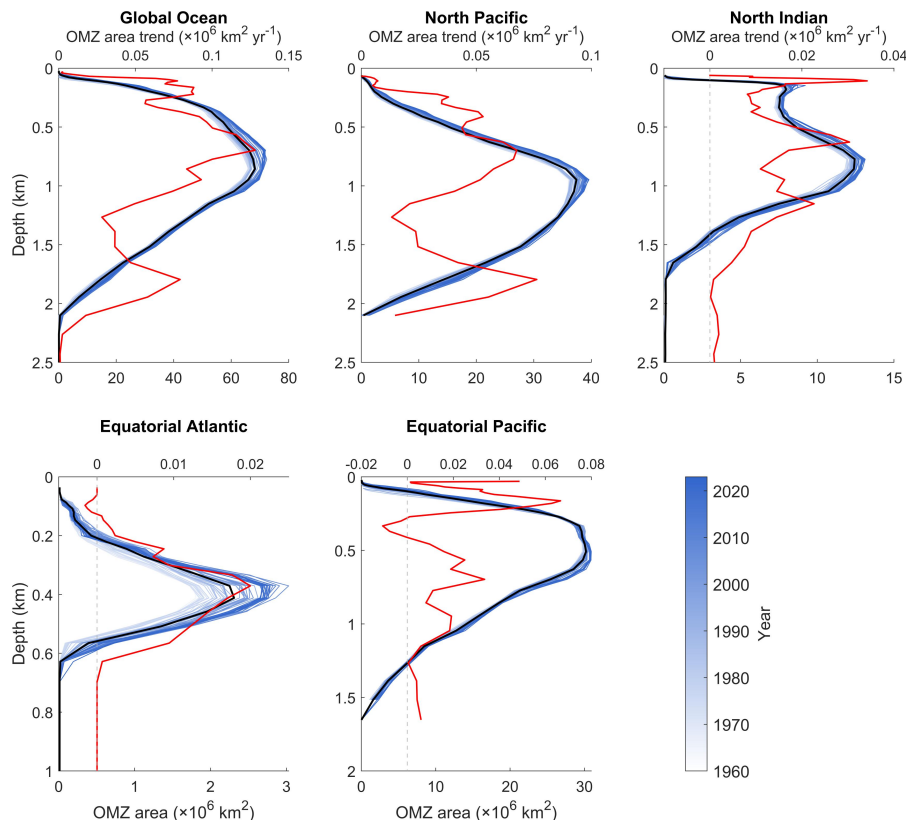408 **4.2 Depth-basin patterns in the OMZ area**

409

410 **Figure 2. Vertical evolution of the OMZ area across major ocean basins during 1960–2023.** Vertical profiles of
411 the annual OMZ area (blue lines; threshold = 60 µmol kg⁻¹) for the global ocean and four major basins: North
412 Pacific, North Indian, Equatorial Atlantic, and Equatorial Pacific. Individual blue curves represent yearly OMZ area
413 profiles, with color shading indicating the year (1960–2023). The black curves show the long-term mean OMZ
414 area at each depth. The red curves denote the linear trend in the OMZ area with depth ($\times$ 10^6 km^2 yr^{-1}),
415 highlighting the depth-dependent expansion or contraction of low-oxygen waters. Here, the North Indian
416 corresponds to the Equatorial Indian (EI) in Figure 1 together with the Bay of Bengal and Arabian Sea.

418 Over the past six decades, the OMZ (DO<60 µmol kg^{-1}) has existed primarily at depths between
419 100 m and 2,000 m, but its vertical structure and magnitude vary strongly between basins (Figure
420 2). In the global mean profile, the total OMZ area increases from the surface to a broad maximum
421 near 800 m and then decreases toward deeper waters. In the North Pacific (NP), the OMZ is
422 thickest, with a wide band of large area between approximately 800 and 1,200 m, which is
423 consistent with slow intermediate-water ventilation and long residence times that allow for
424 respiration to consume oxygen (Karstensen et al., 2008; Paulmier and Ruiz-Pino, 2009). In the
425 North Indian (NI), by contrast, the largest OMZ area is much shallower, between approximately
426 100 and 1,000 m, reflecting a combination of weak thermocline ventilation and strong export
427 production in the Arabian Sea and Bay of Bengal that produces very intense hypoxia (Naqvi et al.,
428 2006; Keeling et al., 2010). The Equatorial Pacific (EP) and Equatorial Atlantic (EA) have thinner
429 OMZ layers centered at approximately 300–600 m. The OMZ in the EP is located primarily in the
430 eastern ocean because of relatively stagnant cyclonic gyres north and south of the equator in the
431 east subsurface layers, which are poorly ventilated (Keeling et al., 2010). In the Atlantic, the OMZ
432 area is much smaller than that in the Pacific, which is consistent with stronger ventilation of the
433 Atlantic thermocline and intermediate waters (Stramma et al., 2008; Talley et al., 2013).

435 These basin differences are also reflected in the vertical profiles of the OMZ extent. OMZ extents
436 have distinct depth profiles across the regions: the NP, EP, and EA are characterized by a single
437 local maximum, whereas the North Indian Ocean (including the Arabian Sea and Bay of Bengal)
438 exhibits two local maxima, suggesting periodic intrusions of oxygen-rich water (Jain et al., 2017;
439 Schmidt et al., 2019; Sarma and Udaya Bhaskar, 2018). The high productivity in the western
440 Arabian Sea region leads to increased oxygen consumption (Acharya and Panigrahi, 2016),
441 whereas the oxygen-rich Somali Current, approximately 500 m deep, introduces oxygen,
442 particularly during summer (Zhang et al., 2022), resulting in weaker OMZs at this depth. Persian
443 Gulf Water (PGW) in the Bay of Bengal contributes to a modest increase in oxygen at 350–450 m
444 (Jain et al., 2017), resulting in a reduced OMZ. These intrusions disrupt the continuity of OMZs,
445 leading to the dual-minima pattern observed in these regions. This phenomenon highlights the
446 complex and dynamic nature of OMZ distribution and its susceptibility to various oceanographic
447 processes.

449 Over the 1960–2023 period, the OMZ area profile gradually expanded across nearly all depths in
450 terms of the global mean and most basins (Figure 2). These changes indicate a significant shift in
451 the vertical distribution and extent of low-oxygen seawater globally over the past six decades.
452 Specifically, the global OMZ extent growth rate was highest at 400–1,000 m because of expansion
453 across all regions, with its peak at 600–700 m due to expansion in the EP and NP. Therefore, while

the largest OMZ extent was approximately 900 m, shifts to the much shallower 600–700 m layer
are likely in the future. After this peak, the horizontal expansion rate of the OMZ decreased, with
the lowest rates occurring at 1,300–1,600 m. However, the expansion rates increased again
beyond 1,600 m because of expansion in the NP.

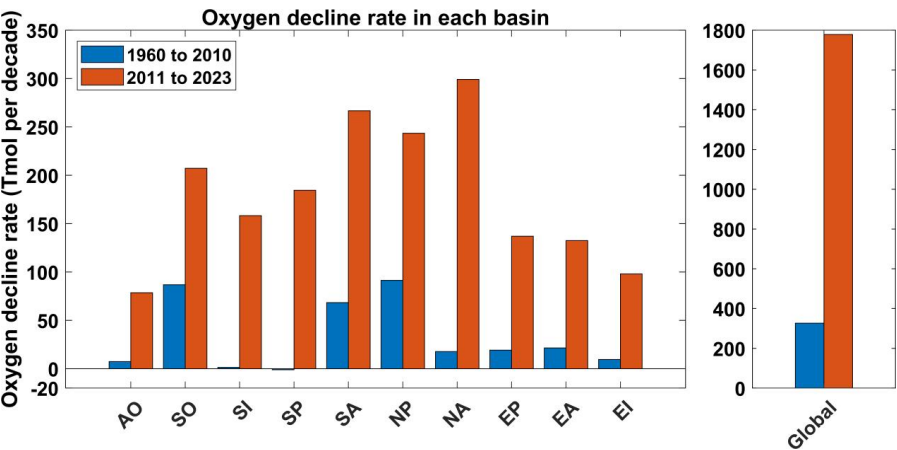**4.3 Basin-scale oxygen content and deoxygenation rates**

Figure 3. Decline in oxygen rates across major ocean basins. Decadal oxygen decline rates are shown for ten
individual ocean basins and for the global ocean and were estimated separately for 1960–2010 (blue) and
2011–2023 (orange).

Deoxygenation was more negative after 2010 across all major ocean basins, indicating stronger
recent oxygen loss over the 1960–2023 record (Figure 3). During the period from 1960 to 2010,
the deoxygenation rates were generally modest. The greatest loss (91.4 $\pm$ 17.7 Tmol decade^{-1})
occurred in the NP, followed by the Southern Ocean (SO) (86.8 $\pm$ 10.5 Tmol decade^{-1}) and
South Atlantic (SA) (68.3 $\pm$ 10.4 Tmol decade^{-1}). In the Southern Indian (SI) and South Pacific
(SP) basins, the deoxygenation trends from 1960 to 2010 were almost negligible. This is highly
likely due to insufficient measurements in the Southern Hemisphere in the early record relative
to those in the Argo era.

In the period after 2010, oxygen loss trends significantly increased across all the basins. The NA
loss increased by more than a factor of 16 to 299.1 $\pm$ 45.8 Tmol decade^{-1}. The SA and NP
exceed 240 Tmol decade^{-1}. The Arctic Ocean (AO) accelerated from near zero to 78.6 $\pm$ 18.1
Tmol decade^{-1}. This recent acceleration of oxygen loss is attributed to amplified warming of
Atlantic inflow from the 2000s to the 2010s, which reduces oxygen solubility and advects
low-oxygen waters into the basin (Wu et al., 2025).

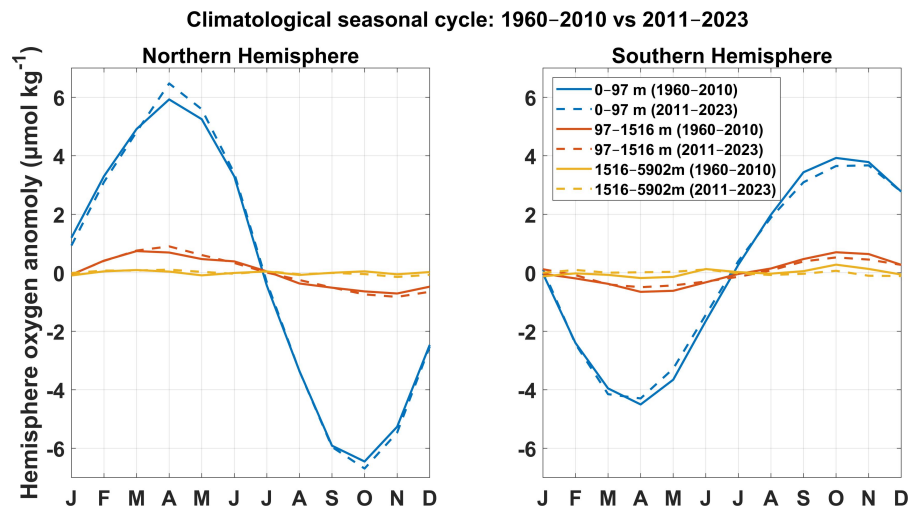**4.4 Hemispheric seasonal variability in dissolved oxygen**

Figure 4. Climatological seasonal cycle of hemispheric mean dissolved-oxygen anomalies. The left panel shows the Northern Hemisphere and the right panel shows the Southern Hemisphere. The blue lines denote the surface layer (0–97 m), the red lines denote the thermocline and intermediate layer (97–1516 m), and the yellow lines denote the deep ocean (1516–5902 m). The solid lines represent anomalies from 1960 to 2010, and the dashed lines represent anomalies from 2011 to 2023.

Along the water column, the seasonal amplitude was strongest in the surface layer, which responds rapidly to the seasonal changes in air–sea gas exchange, surface heating and cooling, and biologically driven production and respiration. In contrast, the seasonal cycles in the thermocline and intermediate ocean (~100–1,500 m) were substantially weaker, with anomalies typically $\pm$ 1 µmol kg^{-1}, and those in the deep ocean (> 1,500 m) were nearly constant throughout the year, with amplitudes below 0.1 µmol kg^{-1} (Figure 4). This rapid vertical decline in seasonality is consistent with the dominant control mechanisms in the ocean interior. Away from the surface, oxygen is mainly controlled by the ventilation of intermediate waters and by the slow remineralization of sinking organic matter. These processes evolve on multiyear to decadal time scales; thus, these water masses respond weakly to the seasonal cycle (Keeling et al., 2010; Talley, 2013). At abyssal depths, water masses are ventilated in high-latitude formation regions and subsequently spread via slow interior circulation; thus, oxygen variability is controlled mainly by large-scale and long-term transport changes (Oschlies et al., 2018).

Comparing 1960–2010 with 2011–2023, the NH surface DO amplitude intensified, whereas the SH weakened. This hemispheric contrast is consistent with the direct dependence of oxygen on temperature and with the positive correlation between changes in the seasonal amplitude of surface DO and SST (Figure S3). In recent decades, the sea surface temperature (SST) seasonal amplitudes in large parts of the Northern Hemisphere have increased, whereas in the Southern Ocean, the SST seasonal cycle has shown robust weakening since the 1950s (Figure S4). Upper-ocean temperature seasonal amplitudes generally increased in the AO and other northern basins but weakened in the Southern Ocean. This pattern is consistent with the opposing NH–SH changes in DO seasonality from our reconstruction.

513 The Northern Hemisphere (NH) displays a larger seasonal amplitude than the Southern
514 Hemisphere (SH), with peak anomalies in the surface and mid-layer ocean approximately 50%
515 greater. A main contributor is the larger NH seasonal temperature range than the SH, which
516 amplifies the seasonal cycle of oxygen solubility and therefore the seasonal cycle of oxygen
517 saturation capacity (Figure S4). Biological processes further enhance these differences. Satellite
518 chlorophyll-a climatology indicates that the seasonal amplitude of phytoplankton biomass is
519 generally larger at mid- and high northern latitudes than at corresponding southern latitudes
520 (Mao et al., 2020), consistent with a stronger seasonal DO response in the NH. Phytoplankton
521 blooms can drive transient surface DO supersaturation in spring, whereas warmer summer
522 conditions can increase heterotrophic respiration (Frajka-Williams et al., 2009; Carstensen et al.,
523 2014). Argo-based analyses show that, although both hemispheres exhibit enhanced
524 upper-ocean stratification in their respective summer seasons, the NH typically shows stronger
525 stratification maxima than the SH (Roch et al., 2023), which limits resupply and intensifies
526 late-summer and early-fall DO minimum (Rippeth et al., 2024).

528 **4.5 Effect of Argo bias correction on the reconstructed oxygen estimates**
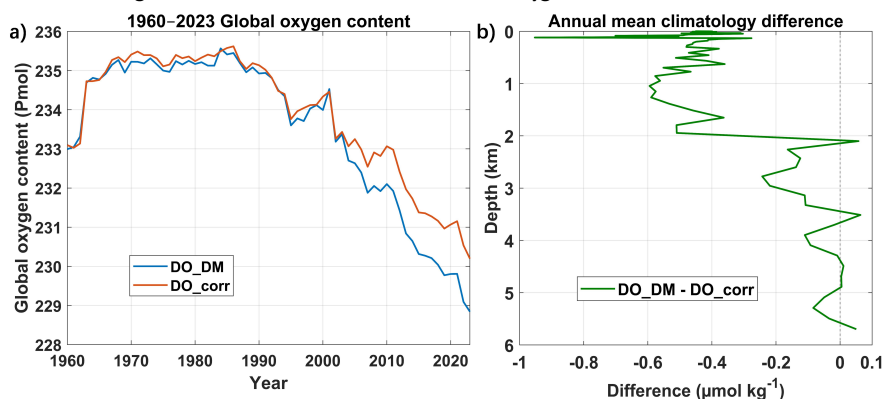

Figure 5. Comparison of global ocean oxygen content and annual mean climatology with and without Argo DO bias correction. (a) Time series of globally integrated ocean oxygen content from 1960 to 2023 based on two reconstructions that use the same machine-learning framework applied to observational oxygen profiles. The blue curve (DO_DM) used oxygen measurements from the CTD, OSD, and delayed-mode Argo profiles. The red curve (DO_corr) used the same inputs but applied a +1.69 $\mu mol\ kg^{-1}$ bias correction to all the Argo DO profiles following Wang et al. (2025). (b) Annual mean vertical profile of the difference between the two reconstructions (DO_DM - DO_corr).

538 The global time series from 1960 to 2023 confirms a long-term and large-scale decline in total
539 dissolved oxygen content (Figure 5a). Over the full analysis period, both our standard and
540 bias-corrected reconstruction methods indicate a persistent decline, with total losses of 5.4 ± 0.5
541 Pmol and 4.1 ± 0.4 Pmol, respectively. This corresponds to overall decreases of 2.3 ± 0.2% and 1.8
542 ± 0.2%, respectively. This magnitude of loss is consistent with prior synthesis estimates of
543 historical deoxygenation, such as approximately 4.8 ± 2.1 Pmol of oxygen loss since 1960 by
544 Schmidtko et al. (2017) and an overall ~2% decrease in oxygen in the late 20th century by Helm et
545 al. (2011).

546 The Argo bias correction produces only modest changes in the reconstructed oxygen fields and
547 does not substantially affect the long-term deoxygenation rates (Figure 5a). Both the standard
548 and the bias-corrected reconstructions strongly agree prior to 2005, when the observations are
549 constrained mainly by ship-based CTD and OSD measurements. After 2005, when the Argo
550 observations became a significant contributor, the reconstruction that incorporates
551 bias-corrected Argo data yielded a slightly higher global mean oxygen content than the
552 uncorrected version did. Consequently, the bias-corrected reconstruction showed a greater
553 global oxygen content in recent years. Vertically, the greatest differences occurred above 2,000 m,
554 where the difference mostly ranged from -0.4 to -0.6 µmol kg^{-1} (Figure 5b), due to dense Argo
555 float sampling and strong optode biases at this depth. Beyond 2,000 m, where sampling mainly
556 comprised sparse ship-based measurements, the difference decreased to -0.2 µmol kg^{-1}, and
557 below approximately 3,500 m, the two reconstructions were almost indistinguishable. In
558 summary, the Argo bias correction improves cross-platform consistency but has only a limited
559 influence on global and basin-scale conclusions drawn from the reconstruction.
560

5 Conclusion and discussion

562 Our study generated the first global 1° ×1° monthly DO dataset from 1960 to 2023, which
563 extends to 5,902 m, achieved through the BLENDR framework. BLENDR integrates six tree-based
564 learners: Random Forest, XGBoost, LightGBM, CatBoost, ERT and Hist_GBT. These models are
565 optimized using Bayesian optimization and combined via dynamic weighting. Our ensemble
566 moves well beyond simpler blends and applies soft weighting that combines each model's global
567 cross-validation skill with local error performance, allowing for the best-performing learner to
568 dominate regionally and depthwise while downweighting those with larger local biases. As a
569 result, our reconstruction achieved lower MAEs and RMSEs than those of any single model or
570 static weight blend on the independent filtered GLODAPv2 dataset and reproduces the
571 large-scale vertical and seasonal structure, including sharp oxycline features and deep ocean
572 signals.
573 The vertical deoxygenation profile revealed accelerating oxygen loss between 150 and 200 m at
574 rates of approximately -0.12 µmol kg^{-1} yr^{-1}, whereas surface decreases remained modest (-0.04
575 µmol kg^{-1} yr^{-1}). Consistent with this, the OMZ area expanded at nearly all depths, with the
576 strongest growth occurring between approximately 400 and 1,000 m and a maximum near
577 600–700 m, which is driven largely by the Equatorial and North Pacific OMZs, whereas weaker yet
578 still positive trends occurred in the deeper North Pacific below 1,600 m. Since 2010, basin-scale
579 trends have accelerated strongly, particularly in the NA and AO, and most other basins have
580 transitioned from weak or negligible trends to substantial oxygen loss, which is consistent with
581 observations of rising temperature, strengthening stratification (Matear et al., 2003; Solomon et
582 al., 2021) and with the deoxygenation of Atlantic inflow feeding the AO (Wu et al., 2025). In the
583 Southern Indian and South Pacific basins, deoxygenation remained weak or even locally positive
584 from 1960 to 2010 (Stramma et al., 2010) but intensified sharply from 2011 to 2023, indicating
585 that these basins shifted from relatively stable oxygen conditions to rapid loss in step with recent
586 upper-ocean warming and circulation changes (Schmidtko et al., 2017; Oschlies et al., 2018).
587 Our analysis of hemispheric DO seasonality revealed that the Northern Hemisphere exhibits

588 seasonal peak anomalies that are approximately 50% greater than those in the Southern
589 Hemisphere in both the surface and thermocline layers. This asymmetry arises primarily from the
590 greater seasonal cycle of upper-ocean temperature in the Northern Hemisphere, which amplifies
591 the seasonal cycle of oxygen solubility, while biological and physical processes further sharpen
592 the extremes: spring phytoplankton blooms drive transient surface supersaturation, and warmer,
593 more strongly stratified summer conditions favor heterotrophic respiration and the development
594 of late-summer to early-fall oxygen minima (Frajka-Williams et al., 2009; Carstensen et al., 2014;
595 Rippeth et al., 2024).

596 A further contribution of this work is the explicit assessment of how Argo oxygen biases
597 propagate into machine-learning reconstructions. By training two parallel ensembles, one using
598 delayed-mode Argo DO together with CTD/OSD profiles (DO_DM) and the other applying a
599 uniform +1.69 μmol kg^{-1} correction to all Argo DO profiles (DO_corr), we directly quantified the
600 sensitivity of global oxygen inventories and trends to this widely used bias adjustment. This
601 comparison highlights that the recent correction in delayed-mode Argo does not significantly
602 affect the deoxygenation trend in global and regional oceans, which enhances the reliability of
603 long-term, observation-constrained reconstructions.

604 We note several limitations and avenues for improvement. The $1° \times 1°$ grid smooths
605 small-scale features such as narrow boundary currents. Even after a constant bias correction was
606 applied to delayed-mode Argo oxygen, residual sensor biases and calibration uncertainties in
607 BGC-Argo profiles still propagated into our training data, especially around steep oxyclines (Bittig
608 et al., 2017; Bittig et al., 2018; Gouretski et al., 2024). Future work should incorporate more
609 precisely calibrated Argo data and finer regional grids.

610 Overall, our dataset offers a unified, long-term view of ocean deoxygenation from the surface to
611 the abyss and, by extending coverage into the bathypelagic realm, fills a critical observational
612 void that enables studies of deep-ocean oxygen dynamics. Packaging in NetCDF with documented
613 uncertainties provides a benchmark for Earth system models and a foundation for impact studies
614 on marine habitats and biogeochemical cycles and invites the community to explore trends,
615 calibrate models and guide policies on ocean health under climate change.

616

Data Availability

618 The reconstructed global monthly dissolved oxygen dataset produced in this study is publicly
619 available in NetCDF format via Zenodo at https://doi.org/10.5281/zenodo.17548659 (Han and
620 Zhou, 2025) under a Creative Commons Attribution 4.0 license. Source DO profile observations
621 were obtained from the International Argo Program and the national programs that contribute to
622 Argo (https://argo.ucsd.edu), the World Ocean Database 2023 (WOD) maintained by the U.S.
623 National Oceanic and Atmospheric Administration (NOAA;
624 https://www.ncei.noaa.gov/products/world-ocean-database), and the Global Ocean Data
625 Analysis Project v2.2023 (GLODAPv2). Environmental predictor fields were drawn from the
626 ORAS5 ocean reanalysis provided by the European Centre for Medium-Range Weather Forecasts
627 (ECMWF; https://cds.climate.copernicus.eu/datasets/reanalysis-oras5).

628

629

630

Author Contributions

M.H. and Y.Z. conceived and designed the study. M.H. performed the research and wrote the initial draft of this paper. M.H., X.X., and Y.Z. reviewed and edited the paper.

Competing interests

The authors declare that they have no competing interests.

References

Acharya S S, Panigrahi M K. Eastward shift and maintenance of Arabian Sea oxygen minimum zone: Understanding the paradox. *Deep Sea Research Part I: Oceanographic Research Papers*, **2016**, 115: 240-252.

Akiba T, Sano S, Yanase T, et al. Optuna: A next-generation hyperparameter optimization framework. *Proceedings of the 25th ACM SIGKDD international conference on knowledge discovery & data mining*, **2019**: 2623-2631.

Bergmeir C, Benítez J M. On the use of cross-validation for time series predictor evaluation. *Information Sciences*, **2012**, 191: 213.

Berman-Frank I, Chen Y B, Gao Y, et al. Feedbacks between the nitrogen, carbon and oxygen cycles. *Nitrogen in the marine environment. Amsterdam The Netherlands: Elsevier Inc*, **2008**, 1537-63.

Bittig H C, Körtzinger A. Update on response times, in-air measurements, and in situ drift for oxygen optodes on profiling platforms. *Ocean Science*, **2017**, 13(1): 1-11.

Bittig H C, Körtzinger A, Neill C, et al. Oxygen optode sensors: principle, characterization, calibration, and application in the ocean. *Frontiers in Marine Science*, **2018**, 4: 429.

Bopp L, Resplandy L, Orr J C, et al. Multiple stressors of ocean ecosystems in the 21st century: projections with CMIP5 models. *Biogeosciences*, **2013**, 10(10): 6225-6245.

Breiman L. Random forests. *Machine learning*, **2001**, 45: 5-32.

Breitburg D, Levin L A, Oschlies A, et al. Declining oxygen in the global ocean and coastal waters. *Science*, **2018**, 359(6371): eaam7240.

Carstensen J, Andersen J H, Gustafsson B G, et al. Deoxygenation of the Baltic Sea during the last century. *Proceedings of the National Academy of Sciences*, **2014**, 111(15): 5628-5633.

Chen T, Guestrin C. Xgboost: A scalable tree boosting system. *Proceedings of the 22nd acm sigkdd international conference on knowledge discovery and data mining*. **2016**: 785-794.

Cocco V, Joos F, Steinacher M, et al. Oxygen and indicators of stress for marine life in multi-model global warming projections. *Biogeosciences*, **2013**, 10(3): 1849-1868.

Deutsch C, Brix H, Ito T, et al. Climate-forced variability of ocean hypoxia. *Science*, **2011**, 333(6040): 336-339.

Dietterich T G. Ensemble methods in machine learning. *International workshop on multiple classifier systems. Berlin, Heidelberg: Springer Berlin Heidelberg*, **2000**: 1-15.

Frajka-Williams E, Rhines P B, Eriksen C C. Physical controls and mesoscale variability in the Labrador Sea spring phytoplankton bloom observed by Seaglider. *Deep Sea Research Part I: Oceanographic Research Papers*, **2009**, 56(12): 2144-2161.

Friedman J H. Greedy function approximation: a gradient boosting machine. *Annals of statistics*, **2001**: 1189-1232.

Gade K. A non-singular horizontal position representation. *The journal of navigation*, **2010**, 63(3): 395-417.

Garcia, Hernan E., et al. *World Ocean Atlas 2023, Volume 3: Dissolved Oxygen, Apparent Oxygen Utilization, Dissolved Oxygen Saturation and 30-year Climate Normal.* **2024**.

Geurts P, Ernst D, Wehenkel L. Extremely randomized trees. *Machine learning*, **2006**, 63: 3-42.

Giglio D, Lyubchich V, Mazloff M R. Estimating oxygen in the Southern Ocean using Argo temperature and salinity. *Journal of Geophysical Research: Oceans*, **2018**, 123(6): 4280-4297.

713 Gouretski V, Cheng L, Du J, et al. A consistent ocean oxygen profile dataset with new quality
714   control and bias assessment. *Earth System Science Data*, **2024**, 16(12): 5503-5530.
715 Gruber N. The dynamics of the marine nitrogen cycle and its influence on atmospheric CO_2
716   variations. *The ocean carbon cycle and climate*. Springer Netherlands, **2004**, 97-148.
717 Gruber N. Warming up, turning sour, losing breath: ocean biogeochemistry under global change.
718   *Philosophical Transactions of the Royal Society A: Mathematical, Physical and Engineering
719   Sciences*, **2011**, 369(1943): 1980-1996.
720 Guryanov A. Histogram-based algorithm for building gradient boosting ensembles of piecewise
721   linear decision trees. *Analysis of Images, Social Networks and Texts: 8th International
722   Conference, AIST 2019, Kazan, Russia, July 17–19, 2019, Revised Selected Papers 8. Springer
723   International Publishing*, **2019**: 39-50.
724 Han M, Zhou Y. Global Monthly Dissolved Oxygen Reconstruction via Bayesian Ensemble Machine
725   Learning. *Zenodo*, **2025**. https://doi.org/10.5281/zenodo.17548659
726 Helm K P, Bindoff N L, Church J A. Observed decreases in oxygen content of the global ocean.
727   *Geophysical Research Letters*, **2011**, 38(23).
728 Huang S, Shao J, Chen Y, et al. Reconstruction of dissolved oxygen in the Indian Ocean from 1980
729   to 2019 based on machine learning techniques. *Frontiers in Marine Science*, **2023**, 10:
730   1291232.
731 Ito T, Cervania A, Cross K, et al. Mapping dissolved oxygen concentrations by combining
732   shipboard and Argo observations using machine learning algorithms. *Journal of Geophysical
733   Research: Machine Learning and Computation*, **2024**, 1(3): e2024JH000272.
734 Jain V, Shankar D, Vinayachandran P N, et al. Evidence for the existence of Persian Gulf water and
735   Red Sea water in the Bay of Bengal. *Climate dynamics*, **2017**, 48(9): 3207-3226.
736 Karstensen J, Stramma L, Visbeck M. Oxygen minimum zones in the eastern tropical Atlantic and
737   Pacific oceans. *Progress in Oceanography*, **2008**, 77(4): 331-350.
738 Ke G, Meng Q, Finley T, et al. Lightgbm: A highly efficient gradient boosting decision tree.
739   *Advances in neural information processing systems*, **2017**, 30.
740 Keeling R F, Körtzinger A, Gruber N. Ocean deoxygenation in a warming world. *Annual review of
741   marine science*, **2010**, 2: 199-229.
742 Kolber Z S, Van Dover C L, Niederman R A, et al. Bacterial photosynthesis in surface waters of the
743   open ocean. *Nature*, **2000**, 407(6801): 177-179.
744 Kwiatkowski L, Torres O, Bopp L, et al. Twenty-first century ocean warming, acidification,
745   deoxygenation, and upper-ocean nutrient and primary production decline from CMIP6
746   model projections. *Biogeosciences*, **2020**, 17(13): 3439-3470.
747 Long M C, Deutsch C, Ito T. Finding forced trends in oceanic oxygen. *Global Biogeochemical Cycles*,
748   **2016**, 30(2): 381-397.
749 Mao Z, Mao Z, Jamet C, et al. Seasonal cycles of phytoplankton expressed by sine equations using
750   the daily climatology from satellite-retrieved chlorophyll-a concentration (1997–2019) over
751   global ocean. *Remote Sensing*, **2020**, 12(16): 2662.
752 Matear R J, Hirst A C. Long-term changes in dissolved oxygen concentrations in the ocean caused
753   by protracted global warming. *Global Biogeochemical Cycles*, **2003**, 17(4).
754 Mishonov A.V., T. P. Boyer, O. K. Baranova, et al. World Ocean Database 2023. C. Bouchard,
755   Technical Ed., *NOAA Atlas NESDIS 97, 206 pp*, **2024**.
756 Naqvi S W A, Naik H, Pratihary A, et al. Coastal versus open-ocean denitrification in the Arabian

757   Sea. *Biogeosciences*, **2006**, 3(4): 621-633.

758   Olsen A, Key R M, Van Heuven S, et al. The Global Ocean Data Analysis Project version 2
759   (GLODAPv2)–an internally consistent data product for the world ocean. *Earth System Science*
760   *Data*, **2016**, 8(2): 297-323.

761   Oschlies A, Brandt P, Stramma L, et al. Drivers and mechanisms of ocean deoxygenation. *Nature*
762   *Geoscience*, **2018**, 11(7): 467-473.

763   Pathak R, Dasari H P, Ashok K, et al. Effects of multi-observations uncertainty and models
764   similarity on climate change projections. *npj Climate and Atmospheric Science*, **2023**, 6(1):
765   144.

766   Paulmier A, Ruiz-Pino D. Oxygen minimum zones (OMZs) in the modern ocean. *Progress in*
767   *oceanography*, **2009**, 80(3-4): 113-128.

768   Prokhorenkova L, Gusev G, Vorobev A, et al. CatBoost: unbiased boosting with categorical
769   features. *Advances in neural information processing systems*, **2018**, 31.

770   Reichstein M, Camps-Valls G, Stevens B, et al. Deep learning and process understanding for
771   data-driven Earth system science. *Nature*, **2019**, 566(7743): 195-204.

772   Rippeth T, Shen S, Lincoln B, et al. The deepwater oxygen deficit in stratified shallow seas is
773   mediated by diapycnal mixing. *Nature communications*, **2024**, 15(1): 3136.

774   Roach, C. J., Bindoff, N. L. Developing a new oxygen atlas of the world's oceans using data
775   interpolating variational analysis. *Journal of Atmospheric and Oceanic Technology*,
776   **2023**, 40(11): 1475-1491.

777   Roberts D R, Bahn V, Ciuti S, et al. Cross-validation strategies for data with temporal, spatial,
778   hierarchical, or phylogenetic structure. *Ecography*, **2017**, 40(8): 913-929.

779   Roch M, Brandt P, Schmidtko S. Recent large-scale mixed layer and vertical stratification maxima
780   changes. *Frontiers in Marine Science*, **2023**, 10: 1277316.

781   Ryther J H. Photosynthesis in the Ocean as a Function of Light Intensity 1. *Limnology and*
782   *Oceanography*, **1956**, 1(1): 61-70.

783   Sampaio E, Santos C, Rosa I C, et al. Impacts of hypoxic events surpass those of future ocean
784   warming and acidification. *Nature Ecology & Evolution*, **2021**, 5(3): 311-321.

785   Sarma V, Udaya Bhaskar T V S. Ventilation of oxygen to oxygen minimum zone due to anticyclonic
786   eddies in the Bay of Bengal. *Journal of Geophysical Research: Biogeosciences*, **2018**, 123(7):
787   2145-2153.

788   Schmidt H, Czeschel R, Visbeck M. Ventilation dynamics of the oxygen minimum zone in the
789   Arabian Sea. *Biogeosciences Discussions*, **2019**, 2019: 1-32.

790   Schmidtko, S., Stramma, L. & Visbeck, M. Decline in global oceanic oxygen content during the
791   past five decades. *Nature*, **2017**, 542(7641): 335-339.

792   Shao J, Huang S, Chen Y, et al. Satellite-based global sea surface oxygen mapping and
793   interpretation with spatiotemporal machine learning. *Environmental Science & Technology*,
794   **2023**, 58(1): 498-509.

795   Sharp J D, Fassbender A J, Carter B R, et al. GOBAI-O2: temporally and spatially resolved fields of
796   ocean interior dissolved oxygen over nearly 2 decades. *Earth System Science Data*, **2023**, 15,
797   4481–4518, https://doi.org/10.5194/essd-15-4481-2023.

798   Shen C. A transdisciplinary review of deep learning research and its relevance for water resources
799   scientists. *Water Resources Research*, **2018**, 54(11): 8558-8593.

800   Solomon A, Heuzé C, Rabe B, et al. Freshwater in the arctic ocean 2010–2019. *Ocean Science*,

801   **2021**, 17(4): 1081-1102.

802   Stramma L, Johnson G C, Sprintall J, et al. Expanding oxygen-minimum zones in the tropical
803   oceans. *Science*, **2008**, 320(5876): 655-658.

804   Stramma L, Prince E D, Schmidtko S, et al. Expansion of oxygen minimum zones may reduce
805   available habitat for tropical pelagic fishes. *Nature Climate Change*, **2012**, 2(1): 33-37.

806   Stramma L, Schmidtko S, Levin L A, et al. Ocean oxygen minima expansions and their biological
807   impacts. *Deep Sea Research Part I: Oceanographic Research Papers*, **2010**, 57(4): 587-595.

808   Talley L D. Closure of the global overturning circulation through the Indian, Pacific, and Southern
809   Oceans: Schematics and transports. *Oceanography*, **2013**, 26(1): 80-97.

810   Tang W, Li Z, Cassar N. Machine learning estimates of global marine nitrogen fixation. *Journal of
811   Geophysical Research: Biogeosciences*, **2019**, 124(3): 717-730.

812   Wang Z, Garcia H E, Boyer T P, et al. Bias Evaluation for Sensor-Based Dissolved Oxygen from CTD
813   and Profiling Floats in the World Ocean Database. *Journal of Atmospheric and Oceanic
814   Technology*, **2025**, 42(10): 1263-1280.

815   Wong A P S, Wijffels S E, Riser S C, et al. Argo data 1999–2019: Two million temperature-salinity
816   profiles and subsurface velocity observations from a global array of profiling floats. *Frontiers
817   in Marine Science*, **2020**, 7: 700.

818   Wu Y, Zheng Z, Chen X, et al. Amplified warming accelerates deoxygenation in the Arctic Ocean.
819   *Nature Climate Change*, **2025**, 15(8): 859-865.

820   Zhang Z, Ma W, Chai F. Role of ocean circulation and settling of particulate organic matter in the
821   decoupling between the oxygen minimum zone and the phytoplankton productive zone in
822   the Arabian Sea: A modeling study. *Frontiers in Marine Science*, **2022**, 9: 927921.

823   Zhou Y, Gong H, Zhou F. Responses of horizontally expanding oceanic oxygen minimum zones to
824   climate change based on observations. *Geophysical Research Letters*, **2022**, 49(6):
825   e2022GL097724.

826

827

828